

# X-Ray Characterization of the Icarus Ultrafast X-Ray Imager

Quinn Looker, Anthony P. Colombo, Mark Kimmel, John L. Porter  
Sandia National Laboratories, Albuquerque, NM, 87123 USA

**Abstract**—Ultrafast x-ray imagers developed at Sandia National Laboratories are a transformative diagnostic tool in Inertial Confinement Fusion and High Energy Density Physics experiments. The nanosecond time scales on which these devices operate are a regime with little precedent, and applicable characterization procedures are still developing. This paper presents pulsed x-ray characterization of the Icarus imager under a variety of illumination levels and timing modes. Results are presented for linearity of response, absolute sensitivity, variation of response with gate width, and image quality.

## I. INTRODUCTION

Experiments in inertial confinement fusion (ICF) and high-energy-density physics (HEDP) involve rapidly changing signals of interest, where interesting physics occurs at the nanosecond time scale or faster [1-4]. The experimental objects typically emit x-rays and other energetic radiation, or x-ray backlighting may be used as a probe. Imaging x-ray detectors are required to utilize these radiation signals to full effect. Due to the challenging environments of ICF and HEDP facilities, time-integrated imagers such as x-ray film or image plate are common. Although they are immune to failure sources such as electronic noise, data quality can suffer when the signal accumulated over an entire experiment is overlaid. For example, ICF target self-emission at stagnation usually eliminates all contrast in at least part of the target area so that no other features in that area can be observed. Inferences of time-dependent behavior can be thus quite challenging or impossible to make. Time-resolved diagnostics exist, but the disadvantages can be significant. Streak cameras image in only one spatial dimension [5], and gated micro-channel plates (MCPs) cast multiple images on different lines of sight and have limited dynamic range [6]. Both can be difficult to calibrate and operate.

The fast-gated Hybrid Complimentary Metal Oxide Semiconductor (hCMOS) technology developed at Sandia National Laboratories offers a transformative diagnostic tool that can simultaneously provide two-dimensional imaging and temporal information on ICF-relevant time scales [7,8]. These compact devices do not require high voltage, perform two-dimensional direct x-ray imaging, and provide multiple frames along an identical line of sight. Framing cameras built around hCMOS detectors have been employed as diagnostics at the Z machine, NIF [9-11], and Omega [12].

The latest generation of hCMOS sensors, named Icarus, provides on-device storage of 4 frames, 0.5 million pixels,  $5 \times 10^5 e^-$  nominal full well, and gate times down to  $\sim 1.5$  ns [13]. The temporal response of Icarus imagers has been previously

characterized using laser light [11,14] and x-rays [15]. However, the imaging performance and capacity for quantitative measurements is largely unexplored.

In this paper, we present the pulsed x-ray characterization of an Icarus sensor. Probe conditions span approximately 2.5 orders of magnitude of x-ray illumination flux as well as multiple camera configurations, which allow us to investigate non-ideal qualities of the sensor arising from the fast time scales on which it operates. We describe the linearity of response and measure the absolute sensitivity of Icarus. We also examine the saturation behavior and the effect of a protection circuit. Finally, we analyze several metrics for the image quality, including response across a sharp edge, background variation, spatial uniformity, and noise characteristics.

## II. EXPERIMENTAL SETUP

The x-ray measurements were conducted at Sandia National Laboratories in the Z-Beamlet/Z-Petawatt Target Bay. The Chaco laser system was used as a pulsed x-ray source. Supplemental measurements were conducted using direct laser illumination of a test diode to better understand the hCMOS photodiode array behavior.

### A. Pulsed X-Ray Source

The Chaco laser system is an amplified Nd:YAG laser frequency-doubled to a wavelength of 532 nm. For this study, each pulse was  $\sim 1$  ns in duration and contained about 1-2 J energy at 532 nm. A pulsed x-ray source was operated by focusing the laser to  $\sim 10$   $\mu$ m spot size at the surface of a Mg foil. The high intensity produces deeply ionized states in the Mg atoms, resulting chiefly in He-like x-ray emission from recombination. For Mg, the bulk of emission is about 1.35 keV per photon [16]. The x-ray emission lasts about 1 ns and is roughly isotropic in the hemisphere facing away from the foil. An annotated view of the vacuum chamber is shown in Fig. 1.

### B. Reference Detectors

Multiple x-ray photodiodes were employed as shot energy monitors. The primary reference was an Opto Diode AXUV100G Si photodiode. The soft x-rays emitted by the Mg foil have an absorption length of 6  $\mu$ m in Si [17], and the detector thickness is approximately 50  $\mu$ m, so essentially no x-ray energy is transmitted through the detector. The dead layer for this detector style is known to be  $< 0.1$   $\mu$ m [18-20], meaning  $< 2\%$  of the x-ray energy is lost at the entrance window. This leaves the cross-sectional area as the limiting dimension for determining detector efficiency. This reference detector was operated behind a steel aperture with a 5 mm diameter opening (smaller than the 10 mm detector size) to constrain the effective

area to a known value. A  $12.7\ \mu\text{m}$  thick Al foil was placed at the aperture to block visible light from reaching the photodiode. The large size of this reference detector creates a large RC component of the readout circuit, resulting in a slow response not suitable for timing measurements.

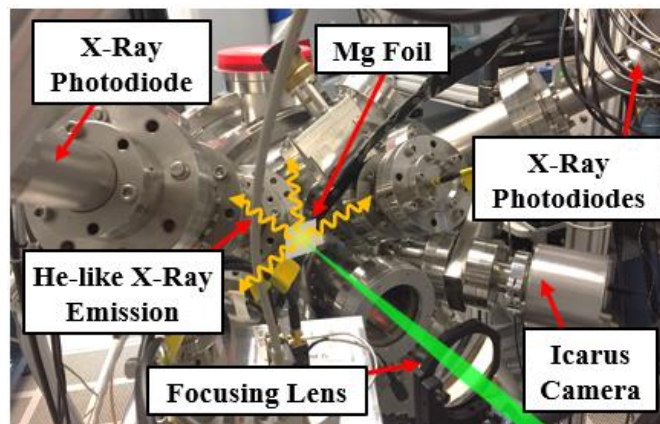


Fig. 1. A photograph of the vacuum chamber used for the pulsed x-ray source. A Mg target foil was located at the center of the vacuum chamber. The laser, illustrated at lower right, is focused onto a small spot at the foil surface to create an x-ray-emitting plasma. Some detector locations are noted in the photograph.

Three alternate reference photodiodes were also employed at a separate line of sight to provide confirmation of the shot energy. One photodiode was composed of  $20\ \mu\text{m}$  thick GaAs and had its active area defined by physical etching [21]. This device is subsequently called the ‘GaAs diode.’ Another photodiode was built on a  $25\ \mu\text{m}$  thick Si layer and had its active detection area physically defined by a polysilicon trench. More details on this device structure can be found in [22]. This device is referred to as the ‘SOI diode,’ indicating its silicon-on-insulator (SOI) device structure. The third alternate reference was a test pixel sub-array to duplicate the photodiode array used on the Icarus sensor. It consisted of a  $10 \times 10$  array of pixels identical in design to those used in the hCMOS device, and the test array was fabricated on the same wafer with hCMOS sensors. The alternate photodiodes also had a  $12.7\ \mu\text{m}$  Al filter to block reflected laser light.

For all photodiodes fielded, the signals and bias levels were carried on  $\sim 10\ \text{m}$  RG-58 cables to PSPL5530B bias tees. The RF output of each channel was connected to an oscilloscope channel with  $50\ \Omega$  termination and  $\sim 3.5\ \text{GHz}$  bandwidth.

### C. hCMOS Configuration

The device under study was an Icarus version 2 (4-frame) sensor [13] with a  $25\ \mu\text{m}$  thick Si detector layer. The hCMOS imager was fielded on its own line of sight with a custom vacuum feedthrough to allow the sensor to be inside the vacuum chamber and the readout electronics to be in air for better heat dissipation. The Icarus sensor had a direct view of the x-ray source through a  $12.7\ \mu\text{m}$  Al foil to block green light from the sensor. It also had a physical mask attached directly to its face to clearly define illuminated and non-illuminated regions. A photograph of the defining mask is shown in Fig. 2. The mask allows large regions of the sensor to be exposed to x-ray illumination, while providing interleaved regions with no x-ray exposure. The  $\sim 35\ \mu\text{m}$  Cu layer blocks all x-ray exposure.

The Icarus imaging array comprises  $1024 \times 512$  pixels with a  $25\ \mu\text{m}$  pixel pitch. A detailed description of the Icarus readout integrated circuit (ROIC) can be found in [13]. A key feature in this investigation was the configurable timing mode, where the exposure window duration and timing are defined by digital command to the ROIC. The sensor always records 4 frames, of exposure duration in the range 2 ns to 38 ns, with a minimum 2 ns period between frames. In this paper, we refer to timing modes as the exposure duration and inter-frame time in ns separated by a ‘/.’ For example, 2/2 timing mode consists of 2-ns exposures separated by 2 ns. Similarly, 38/2 timing is 38-ns exposures separated by 2 ns.

Another ROIC feature investigated was the anti-bloom circuit. Each pixel has a transistor gate that will begin to conduct once the pixel node rises above a threshold voltage, thus preventing too much charge from reaching the frame storage and readout portion of the ROIC. The conductance of this transistor can be varied by a control voltage termed the VAB level.

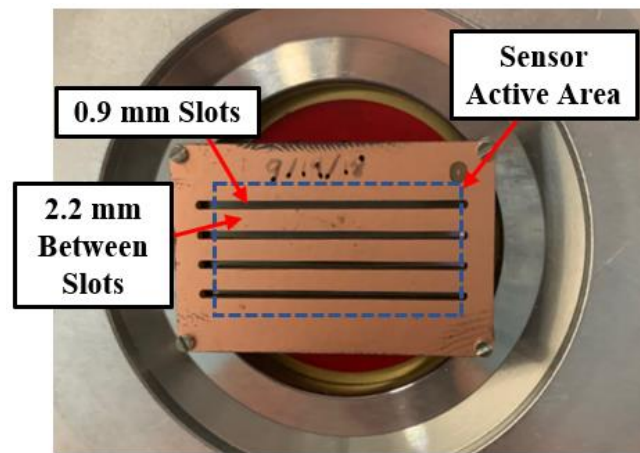


Fig. 2. A photograph of the mask used in front of the hCMOS sensor. The mask material is  $\sim 35\ \mu\text{m}$  copper on a 1.6 mm thick FR-1 epoxy substrate, more than sufficient to completely stop the x-rays in this study. The sensor face is visible through the four open slots, each 0.9 mm wide with 2.2 mm gaps between. The sensor active area is shown by the dashed blue outline.

### D. Test Pixel Diode Measurements

A separate experimental setup was used to measure the hCMOS detector array impulse response. A diode laser producing pulses at 670 nm with  $\sim 100\ \text{ps}$  FWHM was used to directly illuminate the test pixel sub-array. The current pulse from the sub-array was read out directly using a 13 GHz bandwidth oscilloscope. Although the sub-array was also fielded in the pulsed x-ray system, the readout bandwidth was not sufficient to resolve the features of interest. The same device was tested in the laser lab, where short cable lengths ( $\sim 1\ \text{m}$ ) were attainable and a higher bandwidth oscilloscope could be used. Numerous pulses could quickly be acquired and averaged for high waveform quality. The 670 nm light has an absorption depth in Si of  $4.2\ \mu\text{m}$ , similar to the  $6\ \mu\text{m}$  depth for the 1.35 keV x-rays used in the main experimental data.

## III. ANALYSIS METHODS

The primary data set for this study consisted of 242 shots with the pulsed x-ray system. For each shot, the data output

consisted of a waveform for each x-ray photodiode and 4 images from the hCMOS camera. This section describes the analysis steps taken to convert the raw data to physical values of interest.

#### A. Photodiode Waveform Analysis

The oscilloscopes used to record the photodiode waveforms were externally triggered with a signal derived from the laser system. A fast photodiode was used to align the reference diode waveforms from each shot to a common time base. Example waveforms are shown in Fig. 3.

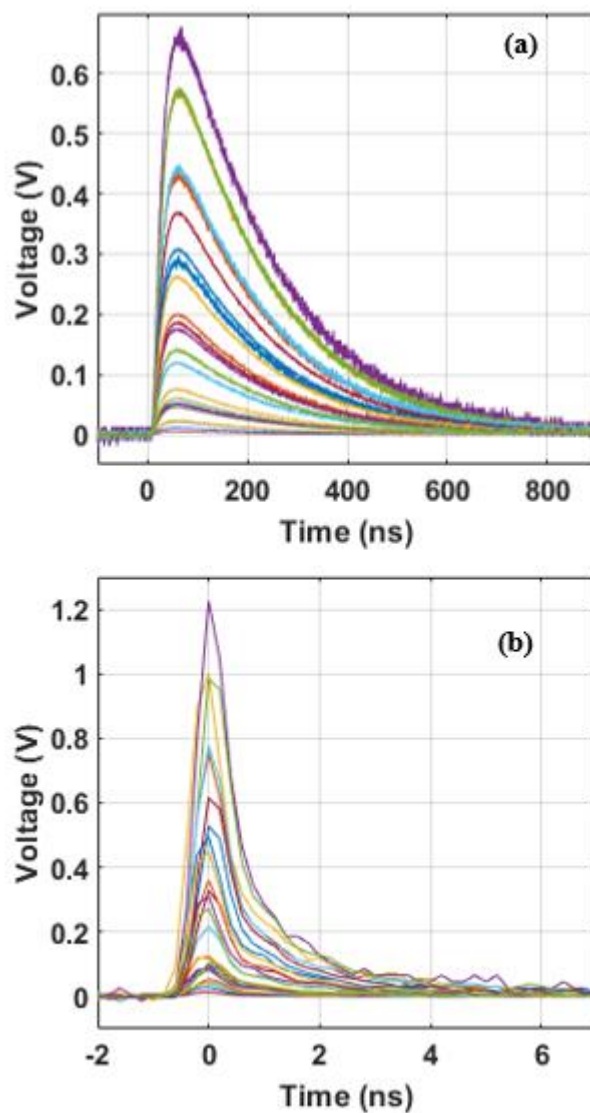


Fig. 3. Example photodiode waveforms. (a) Reference photodiode waveforms used to determine energy emitted by the source. This device was an Opto Diode AXUV100G behind a 5 mm diameter aperture. (b) Fast photodiode waveforms representative of the x-ray emission time history.

Diagnostics were located at four different positions, so they must be related to a common reference point. In this case, the energy emitted by the source was chosen as the common quantity by which to compare the different signals. For a photodiode, the inferred energy emitted by the source is

$$E_{src} = \frac{4\pi d_{det}^2}{A_{det}} \frac{1}{R_{det} Z_{term}} \int V_s(t) dt \quad (1)$$

where  $V_s(t)$  is the sampled voltage in the waveform. The time integral of the waveform divided by the oscilloscope termination  $Z_{term}$  gives the collected charge. Dividing by the detector responsivity  $R_{det}$  (given in C/J) gives the absorbed energy in the detector. This value is derived from the mean electron-hole pair creation energy in Si, 3.62 eV/e-h pair [23], giving a responsivity of 0.274 C/J. Combining with the subtended solid angle of the detector, related to the detector area  $A_{det}$  and detector-source distance  $d_{det}$ , gives the inferred source energy  $E_{src}$ . This process was repeated for each photodiode on each shot.

#### B. Image Analysis

The Icarus sensor image analysis was a multi-step process. Before each x-ray-producing shot, a dark image was acquired with the Icarus sensor. The dark image was subtracted from the on-shot image to remove the fixed-pattern offset (FPO) [14]. Next, four signal regions of interest (ROIs) were selected within the illuminated slot regions of the sensor. Each signal region of interest was accompanied by two background ROIs of identical size, located in the non-illuminated regions immediately on either side of the signal ROI. The average of the two associated background ROIs was subtracted from each signal ROI to remove background levels. Example images from these initial steps are shown in Fig. 4.

The pixel values after fixed-pattern subtraction and background subtraction are the inputs used for the analysis presented in this paper. Each of the four signal ROIs was 1020 rows high by approximately 30 columns wide. For energy measurements, the mean of all pixel values is calculated to form a representative pixel value, which can be used to infer the source energy by

$$E_{src} = \frac{4\pi d_{cam}^2}{A_{pix}} \frac{G_{ADC} q}{R_{det} G_{pix} \epsilon_{pix}} S_{ROI} \quad (2)$$

The mean pixel value for a signal ROI is given by  $S_{ROI}$ . This value is converted to a voltage value by the factor  $G_{ADC}$ , which represents the analog-to-digital converter (ADC) gain for the readout electronics (1 mV per count). The Icarus pixel gain,  $G_{pix}$ , can be used to convert the voltage read value to a number of collected charge carriers. This value was measured at  $1.82 \times 10^{-6}$  V/carrier as described in Section IV.C. The electronic charge  $q$  allows conversion to collected charge. The detector responsivity  $R_{det}$  gives the deposited energy. The Icarus detector is Si, so the same value 0.274 C/J of  $R_{det}$  was used here as for the reference photodiode. The factor  $\epsilon_{pix}$  represents the pixel detection efficiency due to surface conditions such as the metal bias grid and dead layer. This efficiency was 0.907, based on metal grid coverage and a 0.5  $\mu\text{m}$  thick oxide layer covering the detector surface. The solid angle subtended by a pixel is related to the pixel area  $A_{pix}$  ( $25 \mu\text{m} \times 25 \mu\text{m}$ ) and the camera-source distance  $d_{cam}$ .

All image analysis described in the following sections consistently utilizes FPO-corrected images. The method of background correction depends on the measurement type. Where a mean or sum pixel value is used, the quantity is calculated for the signal ROI and associated background ROIs, then the mean background value is subtracted from the signal ROI value. The mean of the four ROI values is used where appropriate. Where distributions of pixels are used, a mean

background ROI is calculated using the two associated background ROIs. This background ROI is then pixel-wise subtracted from the signal ROI to create the final distribution of values.

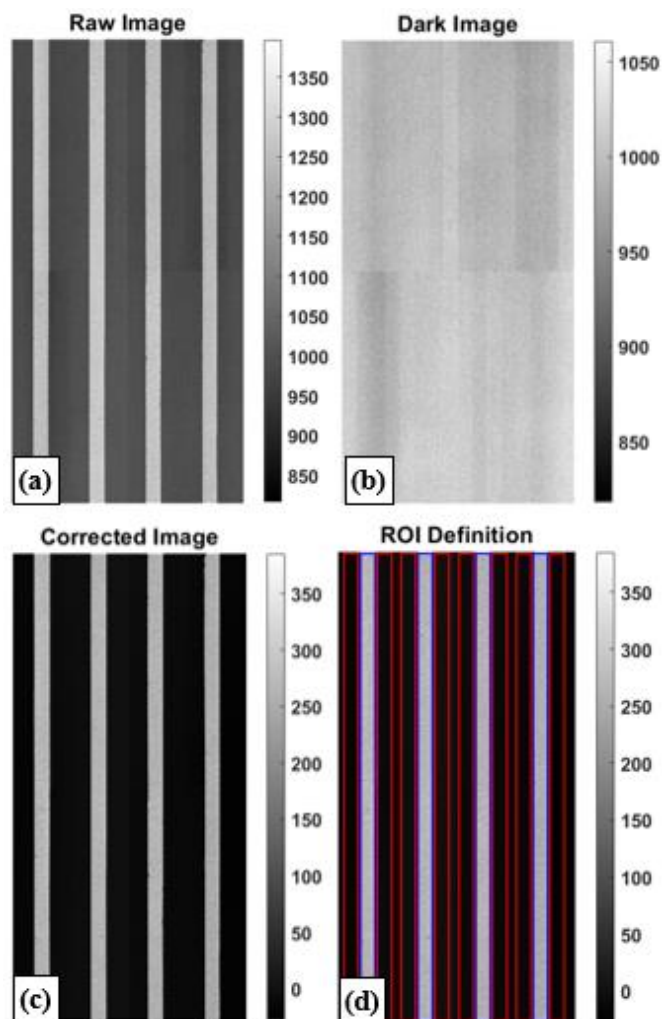


Fig. 4. Example of image processing. (a) Raw image of the x-ray flash. Note the poor contrast and fixed pattern. (b) Dark image acquired before each shot. This is used to correct the undesirable fixed pattern offset. (c) Raw image – dark image. (d) Four Signal ROIs (blue) are defined, each with a pair of background ROIs (red). Intensity values correspond to mV of signal from the sensor.

#### IV. LINEARITY MEASUREMENT

A series of x-ray-producing shots were acquired using the Chaco system with nominally identical timing and spectral content, but varying intensity. The laser amplifier voltages were adjusted to vary the intensity of laser light on the target foil, producing a range of x-ray yields. An x-ray photodiode was used to determine the x-ray energy emitted using Eq. (1), and the Icarus sensor images were analyzed quantitatively to determine inferred x-ray energy using Eq. (2). The result was a measurement of linearity over a certain x-ray intensity range, and the saturation behavior beyond that range as a function of timing mode.

#### A. Photodiode Linearity

The x-ray photodiode linearity was essential to the measurement, so multiple devices were used to demonstrate adequate performance before choosing a source energy measurement methodology. Fig. 5 shows the measured source energy by the reference diode (AXUV100G) and the alternate reference photodiodes.

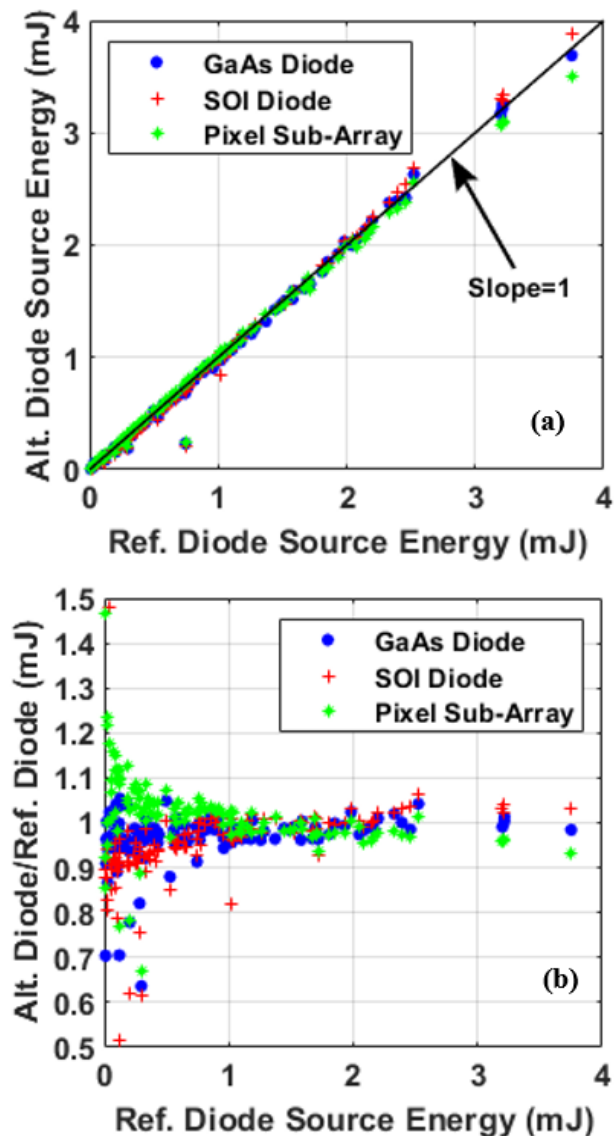


Fig. 5. Reference photodiode source energy measurements. (a) Alternate photodiode measured source energy as a function of primary reference photodiode measured source energy. A line of unity slope is shown as a guide. (b) The ratio of alternate reference diode to primary reference diode measured source energy. At the low end, the smaller sized alternate detectors show increased scatter due to small signal levels. Over most of the energy range, all detectors agreed to within 10%.

The primary and three alternate reference photodiodes represent four completely different device structures at two different locations, and the measured source energy values agree to within 10% over most of the energy range. The three alternates subtend a smaller solid angle of the source than the primary, so there is greater scatter in the measurements due to low signal levels. The GaAs diode gave very consistent results over most of the energy range, probably due to the physical

isolation of its active area. The Si diode had enhanced signal under high illumination, likely the result of some charge carriers being collected through the imperfect polysilicon barrier. The test pixel diode showed reduced levels at high illumination due to slowed carrier collection, described further in Section IV.E.

### B. Timing Mode

The Icarus sensor has digitally configurable exposure times ranging from 2 ns to 38 ns. Though exposure duration should not affect an x-ray measurement fully contained in the exposure time, it was noted that seemingly inconsistent exposure values could be related to timing mode settings. In this data set, the Icarus sensor was operated in 38/2, 8/2, 4/2, and 2/2 timing modes. In each case, the four exposure windows were separated by 2 ns; only the exposure duration varied. The trigger time was adjusted so that the x-ray pulse arrived about 1 ns after the beginning of the second exposure.

The Icarus inferred energy per pixel as a function of incident energy per pixel is shown in Fig. 6. The sensor had a linear response (within 5%) over an energy range equivalent to collection of about 0 to  $10^6$  charge carriers. At high illumination levels, the sensor began to saturate and the detector became less responsive to increases in illumination.

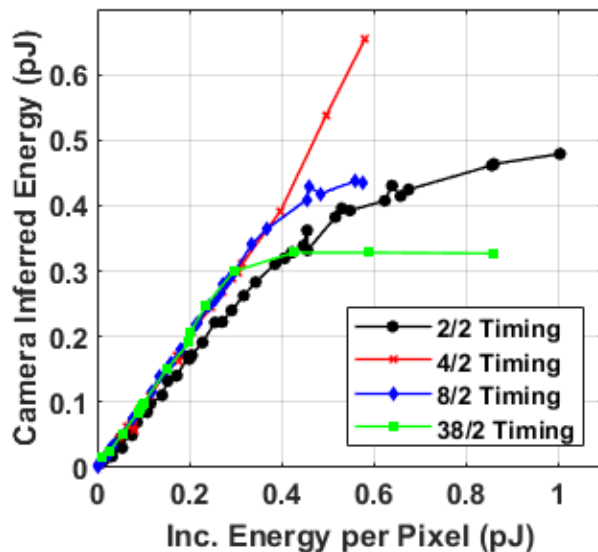


Fig. 6. Inferred energy absorbed per pixel of the Icarus camera as a function of incident energy per pixel. Results are shown for four different exposure durations.

Although the measured pulse energy should be the same for each timing mode, there was an apparent difference in behavior. In the linear range, the 38/2, 8/2, and 4/2 timing modes were in excellent agreement. The 2/2 timing mode was still highly linear, but it suffered an apparent reduced gain. The reasons for this are discussed in Section IV.E. The saturation behavior was significantly different for each timing mode. The 38-ns exposure saturated quickly and had a defined upper limit that did not change with further increases in illumination level. The 8-ns exposure followed a similar pattern, but it reached a higher pixel response saturation limit. The 4-ns exposure did not appear to saturate at all, but it continued to increase its response with increasing illumination. The 2-ns exposure response rolled

off more slowly than the longer timing modes, and its response continued to increase even at the highest levels.

The interpretation of these varying saturation behaviors involves multiple effects. First, we interpret the 2-ns exposure response as being governed by the photodiode array time response. This is explored further in Section IV.E. The 8-ns and 38-ns exposures are limited by the anti-bloom circuit described in Section IV.D, while the 4-ns exposure occupies an intermediate region and is limited by neither mechanism.

### C. Measured Pixel Gain

The Icarus sensor charge gain is a major unknown in a quantitative measurement. The experimental setup allows for a measurement of the Icarus absolute sensitivity. The energy incident on each pixel of the sensor, expressed explicitly in terms of collected carriers is

$$C_{pix} = \frac{d_{det}^2}{d_{cam}^2} \frac{A_{pix}}{A_{det}} \frac{\epsilon_{pix}}{qZ_{term}} \int V_s(t) dt \quad (3)$$

where  $C_{pix}$  is the expected number of collected carriers per pixel. The right-hand side of the equation is rearranged terms from Eqs. (1) and (2).

The camera response is plotted as a function of the number of expected carriers from Eq. (3) in Fig. 7. The black circles show data from the 38/2, 8/2, and 4/2 timing modes only to ensure complete charge collection. A linear fit in the region 0 to  $7 \times 10^5$  e<sup>-</sup> equivalent (0 to 0.43 pJ incident energy) yielded an excellent fit with a slope of  $1.82 \times 10^{-6}$  V/carrier. The error bars in Fig. 7 represent total 1 $\sigma$  error from all sources. The vertical error bars are based on photon shot noise and system read noise. The horizontal error bars are from a variety of sources. The distances  $d_{det}$  and  $d_{cam}$  were carefully measured using a laser distance measure along the line of sight viewed by the diagnostic. The reference photodiode area  $A_{det}$  is well-known by the steel aperture used. A spectral bias in the x-ray flux is unlikely because all diagnostics used filtering cut from the same sheet of Al, and any major discrepancy would appear as a systematic difference among the detectors in Fig. 5. The reference photodiode and Icarus detector array are both Si, so they share the same conversion factor of absorbed energy to charge and the term  $R_{det}$  cancels. The efficiency factor was estimated to be 0.907 based on physical parameters and other x-ray measurements.

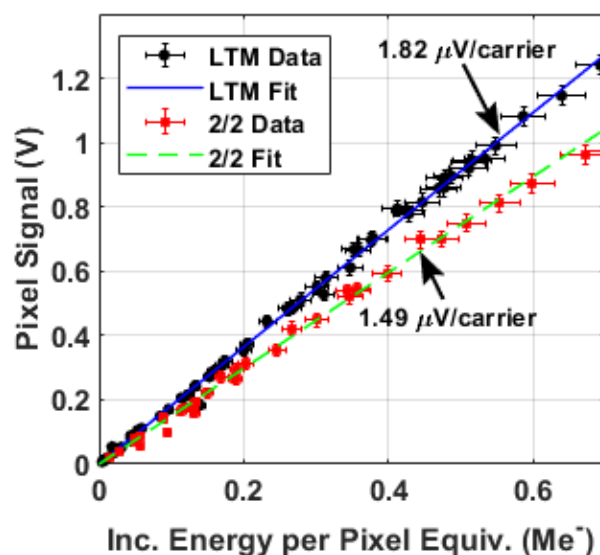


Fig. 7. Measured sensitivity of the Icarus sensor. Black circles represent data from long timing modes (LTM): 38/2, 8/2, and 4/2. The blue line shows a fit to these full charge collection timing modes. The red squares show data from the 2/2 timing mode. The green line is a fit to 2/2 data only.

The Icarus pixel gain has previously been measured at  $1.24 \times 10^{-6}$  V/carrier [15]. This discrepancy in absolute sensitivity could be due to multiple causes. The Hart study focused on 2/2 timing, but this may have resulted in incomplete charge collection and an accompanying apparent reduction in gain. For example, a fit to our 2/2 data results in a slope of  $1.49 \times 10^{-6}$  V/carrier, accounting for much of the discrepancy. Another clear difference between the measurement in this study and that of the Hart study is the illumination level involved. The Hart paper measures the Icarus pixel gain for 1–3 photons at 5.9 keV each, covering the range 0 to 3 fJ. Our data represent 0 to 0.4 pJ absorbed energy per pixel. One possible explanation is that the imager's response has a slight quadratic component that is not easily measured in either data set.

#### D. Protection Circuit

The Icarus sensor include a protection or 'anti-bloom' circuit to prevent damaging over-exposure in the readout circuitry, but its behavior is largely unexplored. The effect of the anti-bloom was studied primarily in the context of saturation behavior. A current-starved transistor with an adjustable control voltage VAB siphons charge away from the photodiode node when it exceeds a voltage level. The behavior of this circuit has not been previously studied for the Icarus sensor.

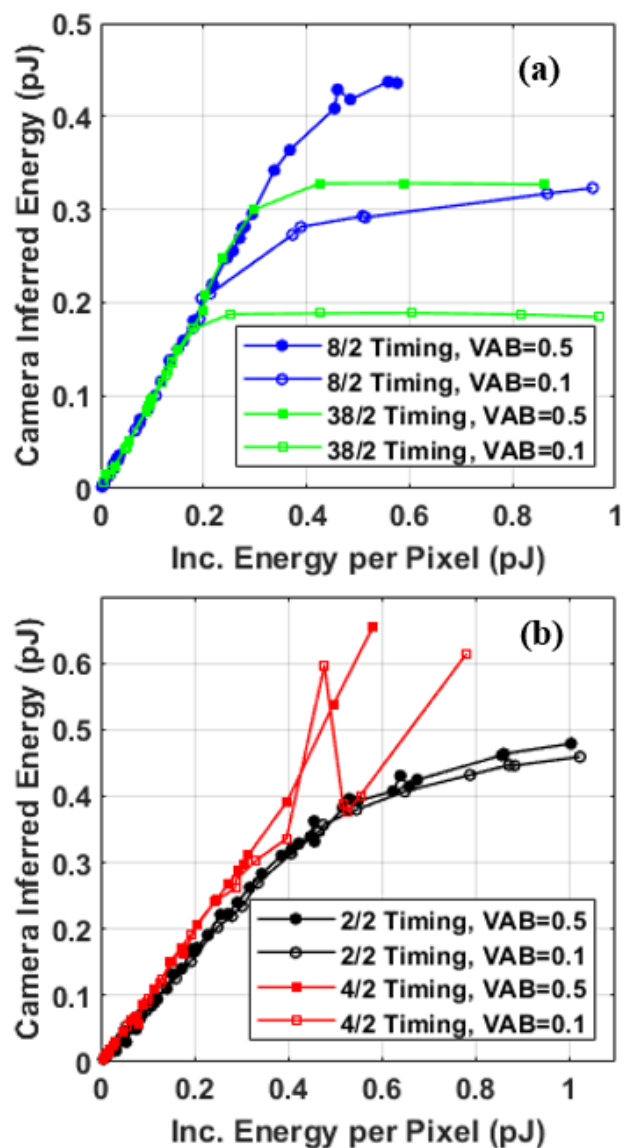


Fig. 8. Varying saturation behavior with timing mode and anti-bloom setting. (a) Icarus sensor inferred energy per pixel as a function of incident energy per pixel for 8/2 and 38/2 timing modes at two different VAB settings. (b) The same for 2/2 and 4/2 timing modes.

We operated our sensor with VAB at 0.5 V (the recommended value) and 0.1 V (maximum anti-bloom effect). Fig. 8 shows the Icarus sensor inferred energy per pixel as a function of incident energy per pixel for the four timing modes at two different anti-bloom settings. For longer timing modes shown in Fig. 8a, the anti-bloom circuit seems to be operating as intended. The camera response flattens at a particular value and remains nearly constant with further illumination. This saturation value varies with the anti-bloom voltage setting. The shorter timing modes, seen in Fig. 8b, have a more complicated saturation behavior. The 2/2 timing mode is nearly unaffected by the anti-bloom setting. Because of this, and the evidence for field collapse we present in the next section, the 2/2 behavior is thought to be entirely due to field collapse in the detector and incomplete charge collection to the storage capacitor. The 4/2 timing mode has a long enough exposure to ensure complete

charge collection, but there seems to be insufficient time for the anti-bloom circuit to engage. The anti-bloom seemed to have no effect at the 0.5 V setting (less anti-bloom effect) and erratic behavior at the 0.1 V setting (more anti-bloom effect).

### E. Field Collapse

Excessive energy deposition in a semiconductor detector can create enough mobile charge in the depletion region to reduce the electric field magnitude acting on those mobile charge carriers [24]. This effect, known as field collapse or plasma effect, slows the detector response under high illumination conditions. A slower than ideal photodiode response is likely responsible for the apparent reduced gain in 2/2 timing mode compared to other timing modes, and further slowing due to field collapse is the best explanation for the 2/2 timing mode saturation behavior.

In all timing modes, the camera exposures were timed so that x-rays arrived during the second of four frames. Fig. 9 shows the frame-to-frame coupling by the ratio of non-exposure frames to the exposure frame. The first frame was exposed before x-rays arrived, so any pattern observed here must be due to coupling in the device rather than any charge collection due to x-ray illumination. As seen in Fig. 9a, the coupling is about 0.1% for all timing modes, and independent of illumination level. The third frame may collect charge from the photodiode that has been delayed due to field collapse. Fig. 9b shows that the coupling is stronger for shorter timing modes and increases substantially at high illumination levels where field collapse may occur.

To better explore this behavior, a test pixel sub-array was illuminated using a pulsed laser and higher fidelity readout as described in II.D. A shorter laser impulse, shorter readout cable length, and higher bandwidth oscilloscope allowed an accurate measurement of the current pulse shape from the Icarus photodiodes at a few different illumination levels. The waveforms, normalized to the same peak height, are shown in Fig. 10a. The legend indicates the equivalent number of electrons per pixel. These waveform shapes were convolved with a 2-ns window to form a normative sensor response. The representative signal during the exposure window was taken near the peak, and the representative signal from the following frame was taken at the peak time plus 4 ns. This formed a predicted third frame to second frame ratio. Fig. 10b shows this prediction overlaid with the measured ratio for 2/2 timing from Fig. 9b.

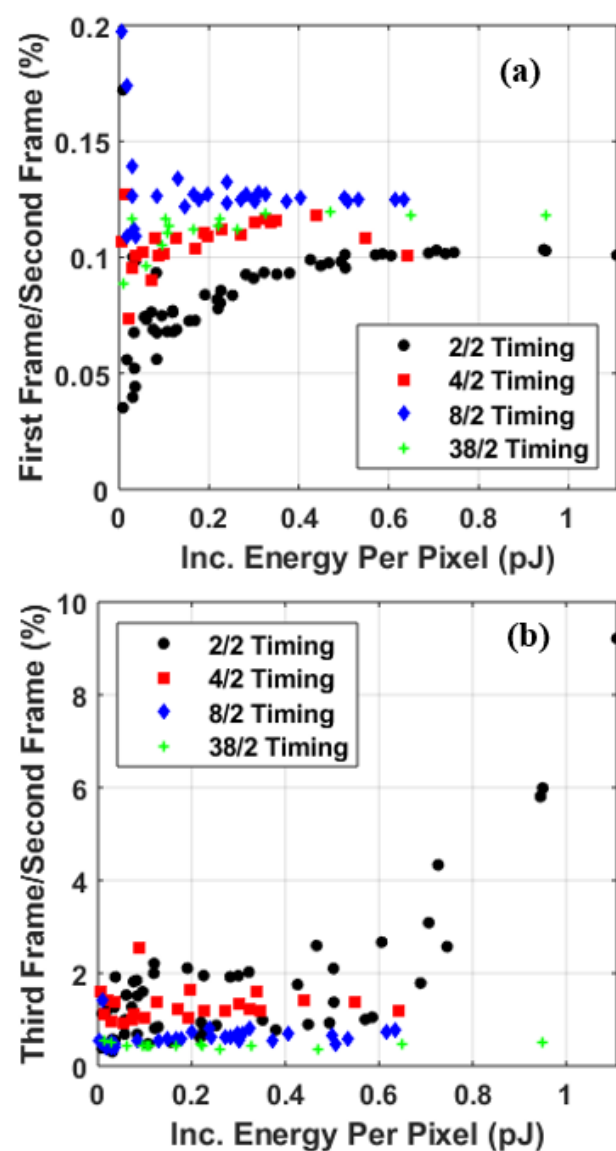


Fig. 9. Frame-to-frame coupling. (a) Ratio of first frame (pre-exposure) to second frame signal as a function of incident energy for the four timing modes. (b) The ratio of third frame (post-exposure) to second frame signal for the four timing modes.

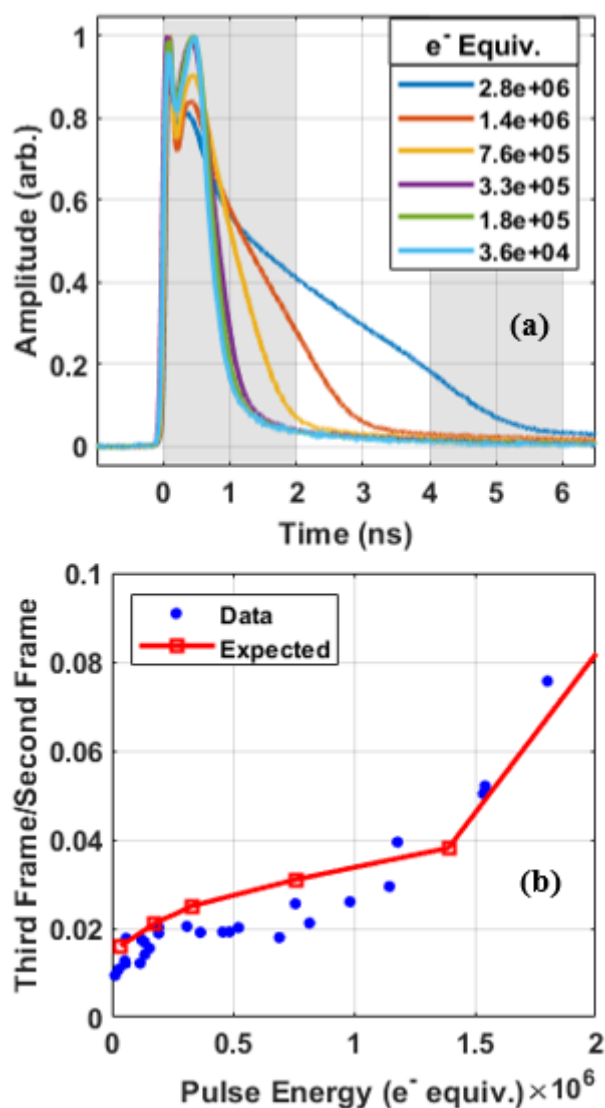


Fig. 10. Test pixel array field collapse measurements. (a) Waveforms acquired with the test pixel array using a pulsed laser setup at six different illumination levels equivalent to the number of electrons per pixel indicated in the legend. Each waveform is normalized to a peak height of one. Nominal imager integration windows are shown in shaded regions. (b) Comparison of measured and expected charge collection in a subsequent 2-ns frame. Blue circles are the measured third frame to second frame ratio in the Icarus x-ray data. Red squares are the predicted behavior using the waveforms in (a).

## V. IMAGE QUALITY

The Icarus device is primarily an x-ray imager, so image quality is of great importance. This section describes analysis of several features affecting image quality.

### A. Step Analysis

A simple measurement of image sharpness is sensor response to a sharp edge. The x-ray blocking mask that was used during the x-ray illumination experiments clearly defines regions illuminated by x-rays and those entirely devoid of illumination. It is possible to roughly interpret the spatial resolution of the imager using the mask edge feature in the images.

The laser was focused to a spot approximately  $10 \mu\text{m}$  FWHM in size at the target foil. The x-ray emission area is thought to

be approximately  $15 \mu\text{m}$  diameter. The imager is 40.7 cm from the source, and the mask is approximately 1.6 mm thick and offset from the sensor surface at  $\sim 1$  mm, making a point source projection of the mask onto the sensor surface a suitable approximation. At a wavelength of  $<1$  nm, diffraction does not significantly degrade the image.

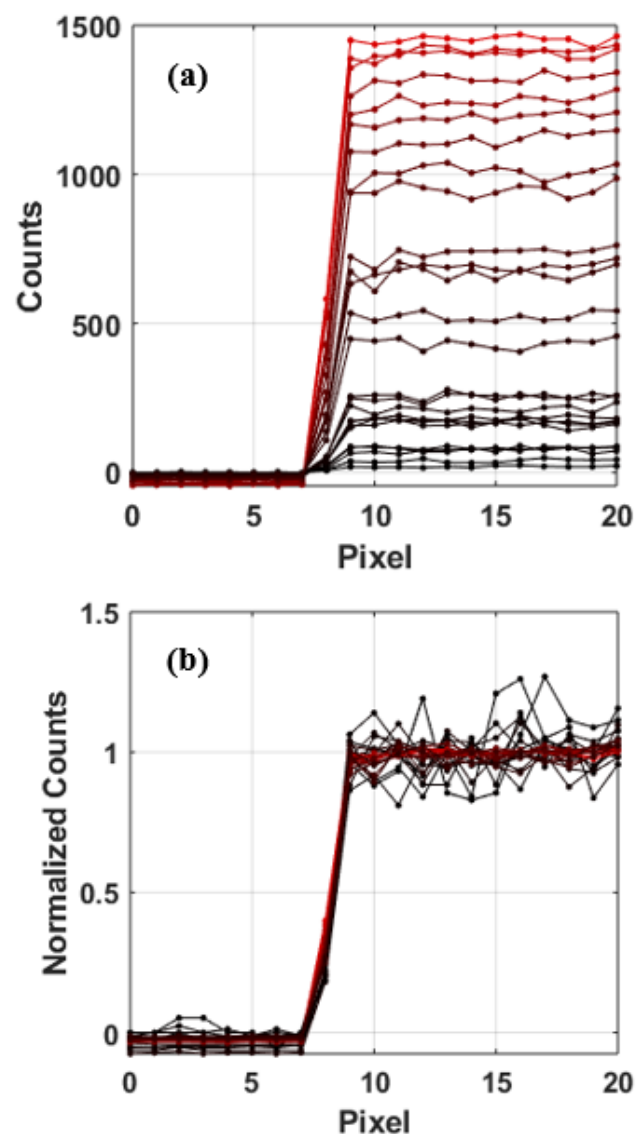


Fig. 11. Lineouts of mask edges. (a) Lineouts for the same set of pixels across a set of images at varying illumination levels. (b) The same lineouts normalized to the same average step height. Greater red color corresponds to increasing x-ray illumination.

The sensor step response was measured by taking a lineout on the same set of 20 pixels for every image in a set. The set of images was chosen to have the same 2/2 timing mode. Fig. 11 shows the set of lineouts in raw and normalized formats. No image blurring is detectable. The intermediate value pixel in the step is due to partial illumination of that pixel. At the highest illumination levels, reduced electric field magnitude could cause enhanced diffusion and blurred images. However, this is not observed. This is consistent with a simple diffusion length  $\sqrt{Dt}$ , where the diffusion coefficient  $D$  is  $\sim 10 \text{ cm}^2/\text{s}$  [25] and the time could be up to 4 ns. The characteristic diffusion length

would be  $<2 \mu\text{m}$ , not significant compared to the  $25 \mu\text{m}$  pixel size.

### B. Image Perimeter Effect

In Icarus, a guard ring that is 4 pixels wide surrounds the  $1024 \times 512$  pixel imaging array. However, due to a packaging error, the guard ring was left floating, meaning the detector material is undepleted. The x-ray illumination mask had slits wider than the imaging array and allowed x-ray illumination on the guard ring at the ends of the slits. It was found that the edge pixels had an enhanced response. Fig. 12 shows an example.

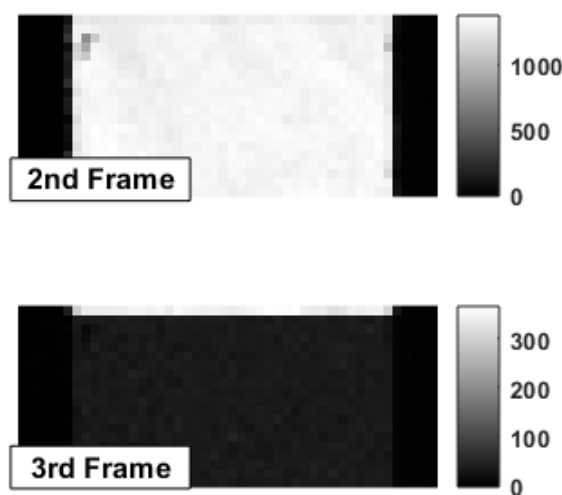


Fig. 12. Example of edge row enhancement. The second frame, during which x-ray illumination occurred, has no enhancement. The following frame's edge pixels are several times the average signal level.

The effect was quantified by taking the average pixel value of the edge row and comparing to the average pixel value of the adjacent rows in the illumination area. It was found that only a single edge row was affected by the guard ring. Two pixels into the imaging array showed no significant enhancement. The enhancement as a function of timing mode gives some insight into its temporal structure. The edge enhancement was defined as mean number of collected charge carriers per pixel on row 1 (the edge row) minus the mean number of collected charge carriers per pixel on row 2 (next to edge row). Fig. 13 shows the edge enhancement for the second and third frames for the different timing modes. Given at least 8 ns of integration time, the edge row collects exactly one extra pixel's charge. The reduced excess for the shorter integration times indicates the collection occurs over several nanoseconds. The following frame edge row excess indicates that collection continues for  $\sim 40$  ns. The likely explanation is diffusion of charge carriers from the undepleted guard ring material.

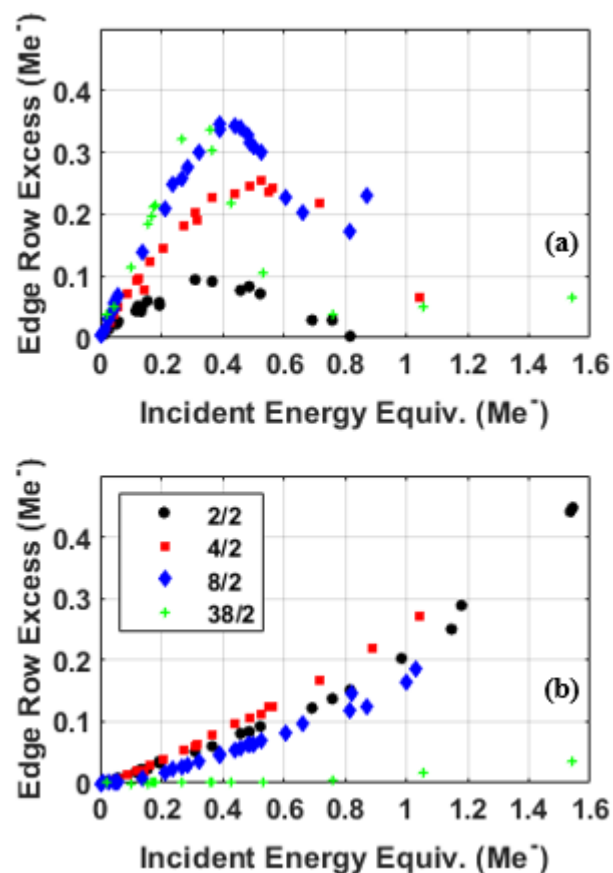


Fig. 13. Edge row excess carrier collection. (a) Second frame (illumination frame) edge row excess collection as a function of incident energy for the various timing modes. (b) The same for the third frame.

### C. Background Behavior

As noted in previous work [14], non-illuminated regions of the Icarus sensor can fluctuate due to effects such as the bias circuit inductance. In this work, we largely removed this effect by keeping large regions of the sensor free of illumination and using them as a reference to subtract the background fluctuations. However, it is worth noting that the magnitude of the effect increases with illumination level. Fig. 14 shows lineouts from each of a set of images at varying illumination levels in 2/2 timing mode. The lineouts were taken near the center of the image. Fig. 14a shows data from the second (illuminated) frame, where increasing red color corresponds to increasing illumination. The non-illuminated pixel values become more negative in proportion to the incident illumination. Fig. 14b shows the following frame. The severity increases with illumination level, but the absolute levels vary significantly.

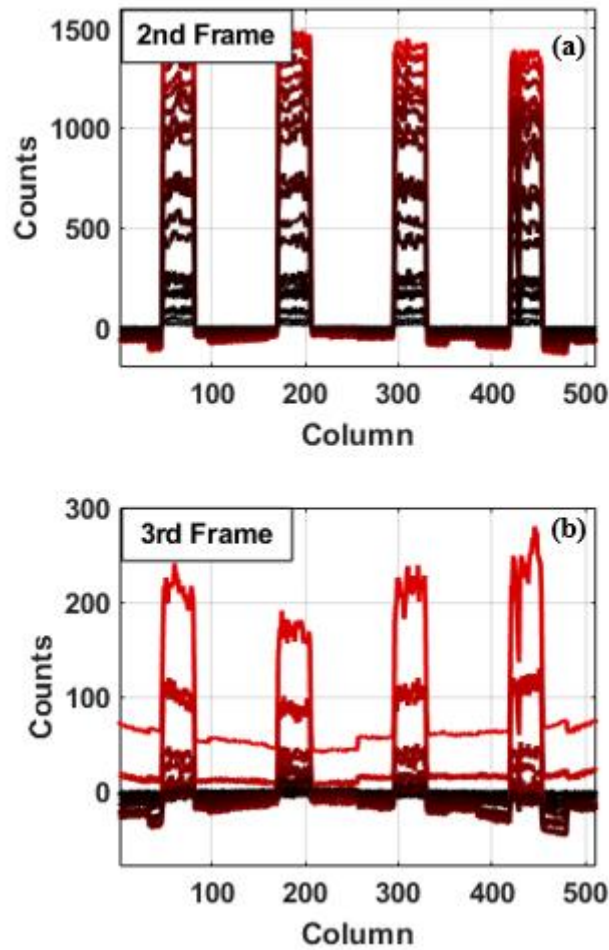


Fig. 14. Non-illuminated region oscillation. (a) Image lineouts near the center for the second (illuminated) frame. (b) The same for the third frame.

#### D. Image Uniformity

Imaging applications benefit from spatial uniformity of sensor response, especially those applications requiring quantitative analysis. We analyzed the large-scale spatial uniformity of a set of images by taking the mean value of each row ( $\sim 30$  pixels) in a single ROI. Fig. 15 shows the ratio of mean row values to the entire ROI mean for all 1024 rows for two ROIs in 38/2 timing mode. The opacity of the plotted line increases with increasing x-ray illumination. Aside from a few rows with dead pixels, the sensor response is uniform to within  $\sim 2\%$  of the mean value.

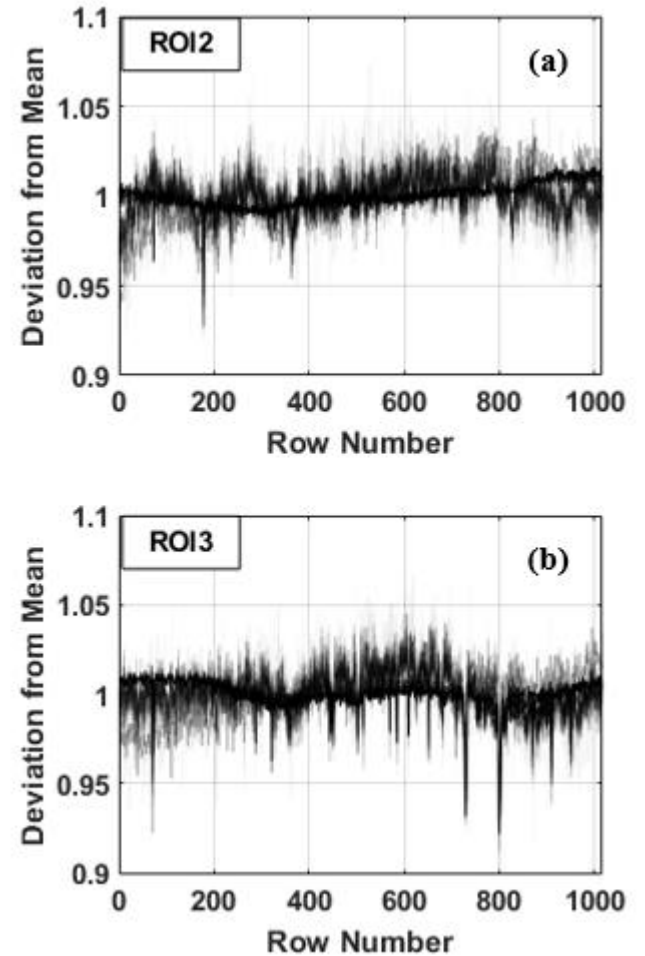


Fig. 15. Uniformity of sensor response across the length of the imaging array. Plotted are mean pixel row values with increasing line opacity corresponding to increasing x-ray illumination for the 38/2 timing mode. (a) Data for ROI2. (b) Data for ROI3.

#### E. Image Noise Analysis

Another factor in image quality is shot noise, which can make images appear grainy due to variations in the number of sensed photons per pixel. There is a physical limit represented by  $\sigma_{shot} = \sqrt{N_{ph}}$ , where  $\sigma_{shot}$  is the standard deviation in pixel value and  $N_{ph}$  is the mean number of photons detected per pixel. Electronic noise in the sensor can further contribute to variation in observed pixel values.

Assuming an average photon energy of 1.35 keV [16], we converted incident energy per pixel to an expected number of photons. Each ROI for each shot contained  $\sim 30,000$  samples that were converted to observed number of photons, and the resulting distribution can be examined. Fig. 16 shows a standard deviation analysis for a set of images in 8/2 timing mode. The black curve indicates the photon shot noise limit, which is the square root of the number of incident photons. The measured standard deviation, indicated by blue circles, increases much more rapidly than expected. Sensor electronic noise should manifest as a constant offset to the square root dependence.

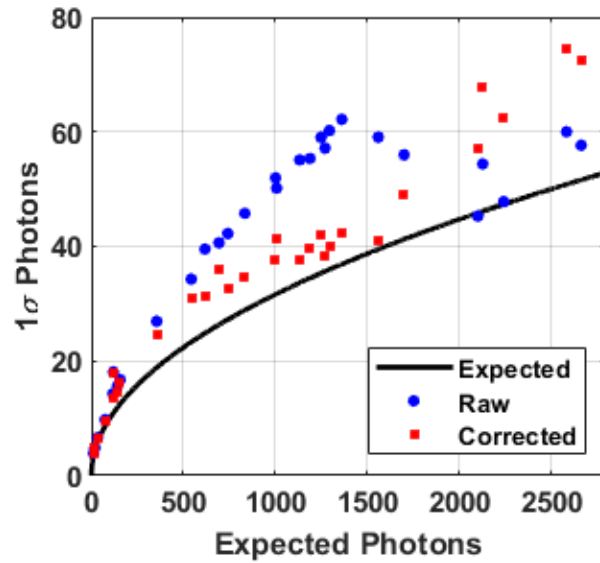


Fig. 16. Image noise analysis with the pixel-wise gain correction for an ROI in 8/2 timing mode. The black curve indicates the expected behavior. The blue circles show the standard deviation in pixel values for the raw image, and the red squares show the same for the gain-corrected image.

A rapid increase in noise as exhibited by the blue dots in Fig. 16 seems to indicate gain variation among the pixels. To test this hypothesis, for each pixel in an ROI, we performed a fit to the linear region to determine the pixel gain. A new, corrected image was created by forcing each pixel to the mean gain of all pixels in the ROI. Performing the same noise analysis on the corrected image recovers the expected square root behavior. The red squares in Fig. 16 show the standard deviation for such a corrected image. The corrected standard deviation matches the expected behavior: photon shot noise  $\sim\sqrt{N_{ph}}$  + constant electronic noise equivalent to a few photons.

The gain variation among pixels could be a property of the sensor or the x-ray illumination pattern. To distinguish between the two possibilities, we acquired a second pulsed x-ray data set nominally identical to the set used to make the plot above. Prior to this second data set, the sensor was physically rotated to give each pixel a different line of sight through the aluminum filter material to the x-ray source. Using the pixel-wise gain correction factors on the second data set, the apparent gain variations increased. This indicates the apparent gain variation among pixels is due to variations in the aluminum foil x-ray attenuation rather than pixel gain variation in the sensor.

## VI. CONCLUSIONS

The Icarus hybrid CMOS imager has been characterized with x-ray pulses of varying intensity. It was found to be linear up to  $10^6$  e<sup>-</sup> collected to within ~3%. Above this illumination level, the saturation behavior varies with timing mode and anti-bloom setting. Field collapse in the detector array appears to occur at high illumination levels, causing a slow imager response comparable to the achievable exposure duration in the integrated circuit. The pixel gain was measured to be  $1.82 \times 10^{-6}$  V/carrier for >2 ns exposures, where full charge collection can

occur in the detector array. The shorter 2/2 timing mode has an apparent gain of  $1.49 \times 10^{-6}$  V/carrier.

The x-ray response is uniform across the array to better than ~2%. Charge carrier diffusion and inter-pixel charge sharing appear to cause no discernable blurring of images. Pixel variation across a large imaging area was found to be nearly consistent with photon shot noise.

## ACKNOWLEDGMENT

Sandia National Laboratories is a multimission laboratory managed and operated by National Technology & Engineering Solutions of Sandia, LLC, a wholly owned subsidiary of Honeywell International Inc., for the U.S. Department of Energy's National Nuclear Security Administration under contract DE-NA0003525.

This paper describes objective technical results and analysis. Any subjective views or opinions that might be expressed in the paper do not necessarily represent the views of the U.S. Department of Energy or the United States Government.

## REFERENCES

- [1] M. R. Gomez, S. A. Slutz, A. B. Sefkow, D. B. Sinars, K. D. Hahn, S. B. Hansen, E. C. Harding, P. F. Knapp, P. F. Schmit, C. A. Jennings et al., "Experimental Demonstration of Fusion-Relevant Conditions in Magnetized Liner Inertial Fusion," *Phys. Rev. Lett.*, vol. 113, p. 155003 (2014).
- [2] D. J. Ampleford, B. Jones, C. A. Jennings, S. B. Hansen, M. E. Cuneo, A. J. Harvey-Thompson, G. A. Rochau, C. A. Cloverdale, A. R. Laspe, T. M. Flanagan et al., "Contrasting physics in wire array z pinch sources of 1-20 keV emission on the Z facility," *Phys. Plasmas*, vol. 21, p. 056708 (2014).
- [3] J. E. Bailey, G. A. Rochau, R. C. Mancini, C. A. Iglesias, J. J. MacFarlane, I. E. Golovkin, J. C. Pain, F. Gilleron, C. Blancard, Ph. Cosse et al., "Diagnosis of x-ray heated Mg/Fe opacity research plasmas," *Rev. Sci. Instr.*, vol. 79, p. 113104 (2008).
- [4] R. D. McBride, M. R. Martin, R. W. Lemke, J. B. Greenly, C. A. Jennings, D. C. Rovang, D. B. Sinars, M. E. Cuneo, M. C. Herrmann, S. A. Slutz et al., "Beryllium liner implosion experiments on the Z accelerator in preparation for magnetized liner inertial fusion," *Phys. Plas.*, vol. 20, p. 056309 (2013).
- [5] J. L. Helfrich and G. F. Blizard, "Streak Camera for Laser Emission Studies," *Rev. Sci. Instr.*, vol. 34, p. 1229 (1963).
- [6] J. D. Kilkenny, P. Bell, R. Hanks, G. Power, R. E. Turner, and J. Wiedwald, "High-speed gated x-ray imagers," *Rev. Sci. Instr.*, vol. 59, p. 1793 (1988).
- [7] L. Claus, L. Fang, R. Kay, M. Kimmel, J. Long, G. Robertson, M. Sanchez, J. Stahoviak, D. Trotter, and J. L. Porter, "An overview of the Ultra-Fast X-ray Imager (UXI) program at Sandia Labs," *Proc. SPIE*, vol. 9591, p. 95910P (2015).
- [8] J. L. Porter, L. D. Claus, L. Fang, R. R. Kay, M. W. Kimmel, A. T. Pomerene, G. A. Robertson, M. O. Sanchez, J. W. Stahoviak, and D. C. Trotter, in The 20<sup>th</sup> Topical Conference on High Temperature Plasma Diagnostics, Atlanta, Georgia, USA, 1-5 June 2014.
- [9] N. E. Palmer et al., "Design and implementation of a gated-laser entrance hole imaging diagnostic (G-LEH-1) at NIF," *Proc. SPIE*, vol. 9591, p. 959106 (2015).
- [10] H. Chen, D. T. Woods, O. S. Jones, L. R. Benedetti, E. L. Dewald, N. Izumi, S. A. MacLaren, N. B. Meezan, J. D. Moody, N. E. Palmer et al., "Understanding ICF hohlraums using NIF gated laser-entrance-hole images," *Phys. Plasmas*, vol. 27, p. 022702 (2020).
- [11] E. R. Hurd, T. Tate, M. S. Dayton, L. Claus, C. E. Durand, M. Johnston, J. M. Di Nicola, A. C. Carpenter, and M. Sanchez, "Time Resolved Near Field (TRNF) diagnostic four-frame nanosecond gated hybrid CMOS image sensor," *Proc. SPIE*, vol. 11114, p. 1111413 (2019).
- [12] W. Theobald, C. Sorce, M. Bedzyk, S. T. Ivancic, F. J. Marshall, C. Stoeckl, R. C. Shah, M. Lawrie, S. P. Regan, T. C. Sangster et al., "The single-line-of-sight, time-resolved x-ray imager diagnostic on OMEGA," *Rev. Sci. Instr.*, vol. 89, p. 10G117 (2018).

This is the author's peer reviewed, accepted manuscript. However, the online version of record will be different from this version once it has been copyedited and typeset.

PLEASE CITE THIS ARTICLE AS DOI:10.1063/1.50004711

- [13] L. Claus, T. England, L. Fang, G. Robertson, M. Sanchez, D. Trotter, A. Carpenter, M. Dayton, P. Patel, and J. L. Porter, "Design and characterization of an improved, 2 ns, multi-frame imager for the Ultra-Fast X-ray Imager (UXI) program at Sandia National Laboratories," *Proc. Of SPIE* vol. 10390, p. 103900A (2017).
- [14] E. R. Hurd, A. C. Carpenter, M. S. Dayton, C. E. Durand, S. R. Nagel, K. Engelhorn, L. Claus, and M. Sanchez, "Performance characterization of a four-frame nanosecond gated hybrid CMOS image sensor," *Proc. Of SPIE* vol. 10763, p. 107630L (2018).
- [15] P. A. Hart, A. Carpenter, L. Claus, D. Damiani, M. Dayton, FJ. Decker, A. Gleason, P. Heimann, E. Hurd, E. McBride et al., "First X-ray test of the Icarus nanosecond-gated camera," *Proc. Of SPIE* vol. 11038, p. 110380Q (2019).
- [16] A. C. Thompson, D. Attwood, E. Gullikson, M. Howells, KJ. Kim, J. Kirz, J. Kortright, I. Lindau, Y. Liu, P. Pianetta et al., "X-Ray Properties of the Elements," in *X-Ray Data Booklet*, 3<sup>rd</sup> ed. 2009.
- [17] B. L. Henke, E. M. Gullikson, and J. C. Davis, "X-ray interactions: photoabsorption, scattering, transmission, and reflection at E=50-30000 eV, Z=1-92," *Atomic Data and Nuclear Data Tables*, vol. 54, no. 2, pp. 181-342, 1993.
- [18] Q. Looker, B. A. Aguirre, M. E. Hoenk, A. D. Jewell, M. O. Sanchez, and B. D. Tierney, "Superlattice-enhanced silicon soft X-ray and charged particle detectors with nanosecond time response," *Nucl. Inst. and Meth. A* vol. 916, pp. 148-153 (2019).
- [19] E. M. Gullikson, R. Korde, L. R. Canfield, and R. E. Vest, "Stable silicon photodiodes for absolute intensity measurements in the VUV and soft x-ray regions," *J. Elec. Spec.* vol. 80, pp. 313-316 (1996).
- [20] G. C. Idzorek and R. J. Bartlett, "Silicon photodiode characterization from 1 eV to 10 keV," *Proc. Of SPIE* vol. 3114, p. 349 (1997).
- [21] Q. Looker, M. G. Wood, P. W. Lake, J. K. Kim, and D. K. Serkland, "GaAs X-Ray Detectors with Sub-Nanosecond Temporal Response," *Rev. Sci. Instr.*, vol. 90, p. 113505 (2019).
- [22] Q. Looker, M. G. Wood, A. Miceli, M. Niraula, K. Yasuda, and J. L. Porter, "Synchrotron Characterization of High-Z, Current-Mode X-Ray Detectors," *Rev. Sci. Instr.*, accepted.
- [23] R. H. Pehl, F. S. Goulding, D. A. Landis, and M. Lenzlinger, "Accurate determination of the ionization energy in semiconductor detectors," *Nucl. Instr. And Meth.*, vol. 59, pp. 45-55 (1968).
- [24] J. Becker, D. Eckstein, R. Klanner, and G. Steinbrück., "Impact of plasma effects on the performance of silicon sensors at an X-ray FEL," *Nucl. Inst. And Meth.* Vol. 615, p. 230 (2010).
- [25] F. Nava, C. Canali, L. Reggiani, D. Gasquet, J. C. Vaissiere, and J. P. Nougier, "On the diffusivity of holes in silicon," *J. Appl. Phys.* Vol. 50, p. 922 (1979).

**X-Ray  
Photodiode**

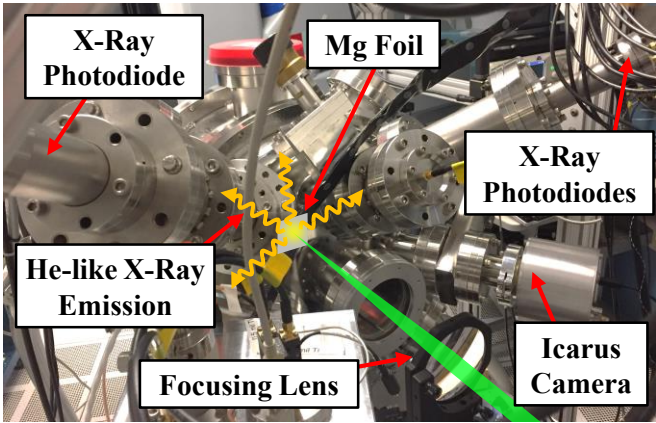
**Mg Foil**

**X-Ray  
Photodiodes**

**He-like X-Ray  
Emission**

**Focusing Lens**

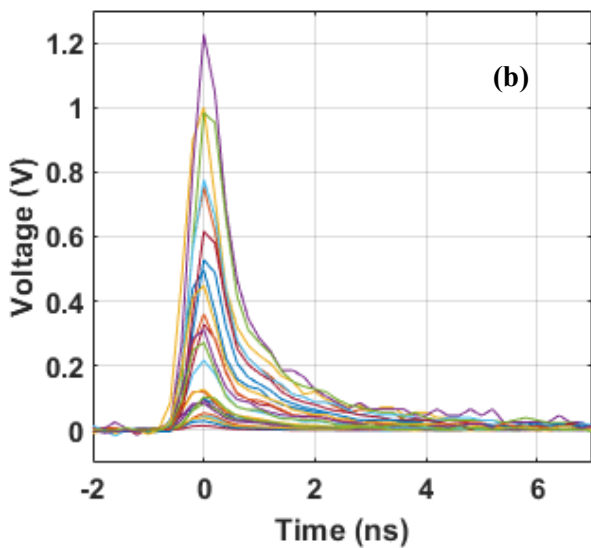
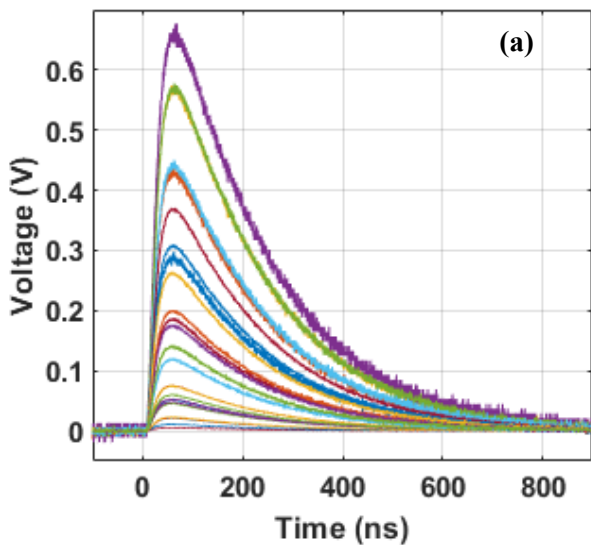
**Icarus  
Camera**



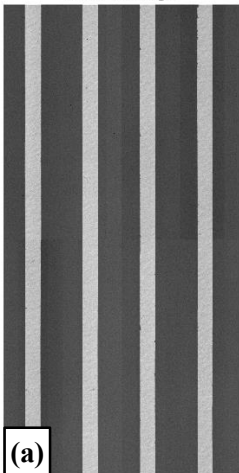
**0.9 mm Slots**

**Sensor  
Active Area**

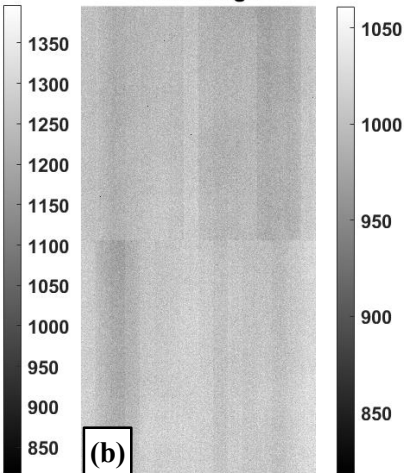
**2.2 mm  
Between  
Slots**



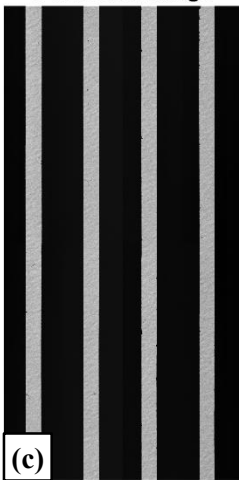
Raw Image



Dark Image



Corrected Image



ROI Definition

